

Positioning via Probabilistic Graphical Models in RIS-Aided Systems with Channel Estimation Errors

Leonardo Terças* and Markku Juntti*

*Centre for Wireless Communications (CWC), University of Oulu, Finland

E-mail: {leonardo.tercas, markku.juntti}@oulu.fi

Abstract—We propose a 6D Bayesian-based localization framework to estimate the position and rotation angles of a mobile station (MS) within an indoor reconfigurable intelligent surface (RIS)-aided system. This framework relies on a probabilistic graphical model to represent the joint probability distribution of random variables through their conditional dependencies and employs the No-U-Turn Sampler (NUTS) to approximate the posterior distribution based on the estimated channel parameters. Our framework estimates both the position and rotation of the mobile station (MS), in the presence of channel parameter estimation errors. We derive the Cramér–Rao lower bound (CRLB) for the proposed scenario and use it to evaluate the system’s position error bound (PEB) and rotation error bound (REB). We compare the system performances with and without RIS. The results demonstrate that the RIS can enhance the positioning accuracy significantly.

Index Terms—Bayesian, RIS, graphical models.

I. INTRODUCTION

Reconfigurable intelligent surface (RIS) have been shown in recent studies to significantly enhance the performance of communications, localization, and sensing systems [1], [2]. RIS consists of a two-dimensional array of numerous small, low-cost, reconfigurable elements capable of manipulating electromagnetic waves [3]. By adjusting the phase shift, amplitude, polarization, and frequency of these elements, RIS can control signal propagation, improving signal quality, coverage, and energy efficiency. This technology has been extensively studied and is expected to be a key enabler for improving communication and sensing in next-generation wireless networks [4]. RIS is particularly important for indoor applications, where it holds great potential to enhance communications quality, improve localization accuracy, and mitigate multipath effects by shaping signal propagation in real time [5], [6].

Among the many studies on RIS, RIS-aided or RIS-enabled positioning stands out. In these studies, RIS acts as an anchor with a known state (i.e., location and orientation) and exploits the reflected signals from the surface to improve or assist mobile station (MS) localization. However, implementing indoor RIS-aided mmWave multiple-input multiple-output (MIMO) systems faces several challenges, including managing multipath reception, obstructed line-of-sight (LOS), and the high density of scatterers and clutter. Channel estimation is particularly complex in mmWave systems due to their susceptibility to blockage and attenuation, making it difficult to provide accurate feedback for optimal beamforming and signal reflection in dynamic indoor environments [5], [7]. Many works have derived the Cramér–Rao lower bound (CRLB) and

the position error bound (PEB) for two- and three-dimensional localization problems in scenarios containing RIS [8], [9].

The potential of RIS-aided mmWave systems to enhance localization capabilities alongside communications by utilizing sparse reconstruction algorithms for high-resolution channel estimation in 3D indoor environments has been studied in [6]. A joint 3D localization of a hybrid reconfigurable intelligent surface and a user, utilizing a multistage approach for 6D parameter estimation (position and rotation) has also been explored in [8], along with the derivation of the CRLB for the system. In [9], Liu *et al.* investigate the CRLB for location estimation error in multiple-RIS-aided mmWave positioning systems, focusing on the PEB and rotation error bound (REB). Zhang *et al.* [10] propose a single-base-station localization method for multiple RIS in non-line-of-sight (NLOS) 3D environments by estimating the position of the user using time of arrival, angle of arrival, and time difference of arrival.

Conventional optimization-based algorithms like non-linear least squares and maximum likelihood estimators [8]–[10] have been widely used for user location estimation, but they often require extensive measurements or iterations to achieve accuracy, which may not be feasible in some applications. In contrast, Bayesian inference, using probabilistic graphical models, offers an alternative by representing complex relationships through probability rules and incorporating uncertainties and prior knowledge. This method estimates position by sampling from the joint posterior distribution, providing a distinct approach to target positioning. In this paper, we propose a 6D Bayesian-based localization framework to estimate both the position and rotation of a MS in an RIS-aided indoor environment. Our main contribution is the development of this framework, which integrates Bayesian inference with probabilistic graphical models to improve location and orientation accuracy. Additionally, we perform a comparative analysis with scenarios that exclude RIS, focusing on the performance gains in both position and rotation estimation introduced by the presence of RIS. To assess the proposed framework’s performance, we analyze the cumulative distribution function (CDF) of the estimation error, along with the PEB and REB derived from the CRLB.

II. SYSTEM MODEL

A. Coordinate System

The coordinate system considered in this work is defined in [11]. The Cartesian representation of a point (x, y, z) on the unit sphere are determined by its spherical coordinates

described by $(\rho = 1, \theta, \phi)$, where ρ represents the unit radius, θ denotes the zenith angle measured from the positive z -axis, and ϕ indicates the azimuth angle measured from the positive x -axis within the x - y plane. The Cartesian coordinates are expressed as follows

$$\hat{\rho} = \begin{bmatrix} x \\ y \\ z \end{bmatrix} = \begin{bmatrix} \rho \sin(\theta) \cos(\phi) \\ \rho \sin(\theta) \sin(\phi) \\ \rho \cos(\theta) \end{bmatrix}, \quad (1)$$

where this coordinate point represents a location in the global coordinate system (GCS), the spherical coordinates can be computed as $\theta = \arccos(z)$ and $\phi = \arctan 2(y, x)$ ¹. Considering an arbitrary 3D rotation, it is possible to compute its corresponding position in the local coordinate system (LCS). The composite rotation matrix representing any arbitrary 3D rotation is given by (2)

$$\mathbf{R} = \mathbf{R}_z(\alpha) \mathbf{R}_y(\beta) \mathbf{R}_x(\gamma), \quad (2)$$

where α is the bearing angle, β is the downtilt angle, and γ is the slant angle. The matrices $\mathbf{R}_z(\alpha)$, $\mathbf{R}_y(\beta)$, and $\mathbf{R}_x(\gamma)$ represent the rotations around the z -axis, y -axis, and x -axis, respectively, and are given by

$$\mathbf{R}_z(\alpha) = \begin{bmatrix} \cos(\alpha) & -\sin(\alpha) & 0 \\ \sin(\alpha) & \cos(\alpha) & 0 \\ 0 & 0 & 1 \end{bmatrix}, \quad \mathbf{R}_y(\beta) = \begin{bmatrix} \cos(\beta) & 0 & \sin(\beta) \\ 0 & 1 & 0 \\ -\sin(\beta) & 0 & \cos(\beta) \end{bmatrix},$$

$$\mathbf{R}_x(\gamma) = \begin{bmatrix} 1 & 0 & 0 \\ 0 & \cos(\gamma) & -\sin(\gamma) \\ 0 & \sin(\gamma) & \cos(\gamma) \end{bmatrix}. \quad (3)$$

The relationship between the spherical angles (θ, ϕ) in the GCS and the spherical angles (θ', ϕ') in the LCS, considering the rotation defined by (2), are expressed as follows

$$\theta' = \arccos \left(\begin{bmatrix} 0 \\ 0 \\ 1 \end{bmatrix}^T \mathbf{R}^T \hat{\rho} \right), \quad \phi' = \arctan 2 \left(\begin{bmatrix} 0 \\ 1 \\ 0 \end{bmatrix}^T \mathbf{R}^T \hat{\rho}, \begin{bmatrix} 1 \\ 0 \\ 0 \end{bmatrix}^T \mathbf{R}^T \hat{\rho} \right). \quad (4)$$

B. Signal Model

We consider a 3D indoor environment, as depicted in Fig. 1, which includes a multi-antenna base station (BS), a RIS, and a MS. These are located at $\hat{\rho}_B = [x_B, y_B, z_B]^T$, $\hat{\rho}_R = [x_R, y_R, z_R]^T$, and $\hat{\rho}_M = [x_M, y_M, z_M]^T$, and rotated $\mathbf{r}_B = [\alpha_B, \beta_B, \gamma_B]$, $\mathbf{r}_R = [\alpha_R, \beta_R, \gamma_R]$, and $\mathbf{r}_M = [\alpha_M, \beta_M, \gamma_M]$, respectively. We assume a uniform planar array (UPA) for the antennas/elements, which are parallel to the x - z plane. The orthogonal frequency division multiplexing (OFDM) downlink received signal model at the MS, where n and t denote the OFDM subcarrier and symbol index, respectively, is assumed as follows:

$$y_{n,t}^{u_1, u_2} = \sum_{v_1, v_2} (H_{n, u_1, u_2}^{BM, v_1, v_2} + H_{n, t, u_1, u_2}^{BRM, v_1, v_2}) x_{n,t}^{v_1, v_2} + w_{n,t}^{u_1, u_2}, \quad (5)$$

where \mathbf{H}^{BM} represents channel tensor of the direct communication link between the BS and the MS, \mathbf{H}^{BRM} is the channel tensor of the link between the BS, RIS and the MS, \mathbf{x} is the transmitted pilot tensor, and $w_{n,t}^{u_1, u_2}$ is additive white Gaussian noise (AWGN) following $\mathcal{CN}(0, N_0)$. Furthermore, the v_1 and v_2 indices represent the transmit antennas along each

¹The arctan2 function computes the angle between the positive x -axis and the point (x, y) in the Cartesian plane. The result is in the range $[-\pi, \pi]$.

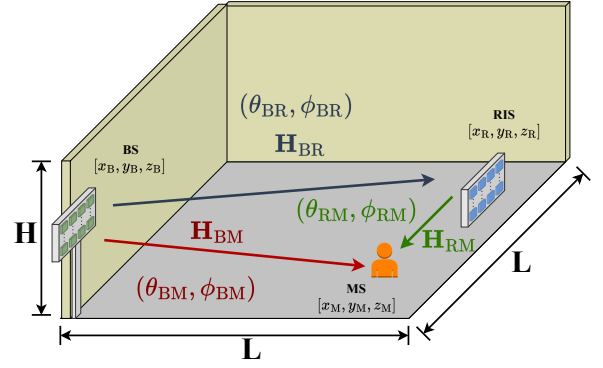


Fig. 1. Indoor scenario for RIS-aided mmWave MIMO systems. The environment is modeled as a square with sides of length (L) and height (H).

dimension (assuming a uniform rectangular array) and go up to $N_{B_1} - 1$ and $N_{B_2} - 1$, respectively. Similarly, the u_1 and u_2 indices are related to the receive antennas.

The BS-MS channel tensor, denoted as \mathbf{H}^{BM} , is complex valued of size $N_c \times N_{M_1} \times N_{M_2} \times N_{B_1} \times N_{B_2}$, where N_c is the number of subcarriers, N_{B_1} and N_{B_2} represent the number of antennas along each direction of the rectangular array of the BS (similarly defined for N_{M_1} and N_{M_2} at the MS). Its structure is modeled as a LOS channel

$$H_{n, u_1, u_2}^{BM, v_1, v_2} = b_{BM} e^{jn\omega_{BM}} e^{ju_1\psi_1^{BM}} e^{ju_2\psi_2^{BM}} e^{jv_1\varsigma_1^{BM}} e^{jv_2\varsigma_2^{BM}}, \quad (6)$$

where the ψ^{BM} and the ς^{BM} are, respectively, the angle of arrival and angle of departure spacial frequencies from the BS to MS direct link. These are defined in the following fashion

$$\psi_1^{BM} = \pi \sin \theta'_{MB} \cos \phi'_{MB}, \quad \psi_2^{BM} = \pi \cos \theta'_{MB}, \quad (7)$$

$$\varsigma_1^{BM} = \pi \sin \theta'_{BM} \cos \phi'_{BM}, \quad \varsigma_2^{BM} = \pi \cos \theta'_{BM}, \quad (8)$$

where θ_{BM} and ϕ_{BM} represent the zenith and azimuth departure angles from the BS to the MS, respectively. Similarly, θ_{MB} and ϕ_{MB} represent the zenith and azimuth arrival angles to the MS from the BS, respectively. Furthermore,

$$\omega_{BM} = -2\pi(\tau_{BM} + \tau_0)f_{sc}, \quad (9)$$

where τ_{BM} is the propagation delay between BS and MS, τ_0 is the clock timing offset, and f_{sc} is the subcarrier spacing. The propagation path loss, denoted as b_{BM} , is given by

$$b_{BM} = \sqrt{\frac{c}{f_c 4\pi d_{BM}}} e^{j\angle b_{BM}}, \quad (10)$$

where d_{BM} is the distance between BS-MS, c is the speed of light, f_c is the central frequency, and $\angle b_{BM}$ is the path phase contribution.

The BS-RIS-MS channel is derived by cascading the BS-RIS channel \mathbf{H}^{BR} and the RIS-MS channel \mathbf{H}^{RM} . The compound channel is modeled in the following way

$$H_{n, t, u_1, u_2}^{BRM, v_1, v_2} = b_{BR} b_{RM} e^{jn\omega_{BRM}} e^{ju_1\psi_1^{RM}} e^{ju_2\psi_2^{RM}} \left(\sum_{k_1, k_2} \Omega_{k_1, k_2, t} e^{jk_1\vartheta_1} e^{jk_2\vartheta_2} \right) e^{jv_1\varsigma_1^{BR}} e^{jv_2\varsigma_2^{BR}}, \quad (11)$$

where the b , ψ , and ς parameters are analogous to those in (6). Also, $\vartheta_1 = \psi_1^{BR} + \varsigma_1^{RM}$, $\vartheta_2 = \psi_2^{BR} + \varsigma_2^{RM}$, and

$\Omega_{k_1, k_2} = e^{j\omega_{k_1, k_2, t}^{\text{RIS}}}$ is the RIS phase shift at element (k_1, k_2) and symbol t . Finally, $\omega_{\text{BRM}} = -2\pi(\tau_{\text{BR}} + \tau_{\text{RM}} + \tau_0)f_{\text{sc}}$. The RIS is rectangular with dimensions $N_{\text{R}_1} \times N_{\text{R}_2}$, thus the total number of elements is $N_{\text{R}} = N_{\text{R}_1} N_{\text{R}_2}$.

III. FUNDAMENTAL BOUNDS

In this paper, we assume that channel estimation (CE) is applied, allowing us to retrieve near-perfect channel estimates with some estimation error. This could be achieved, for example, by leveraging various mechanisms such as error correction, feedback techniques, and advanced signal processing methods, including Deep Neural Networks and sparse signal recovery [12]–[15]. The estimated channel parameters are given by

$$\hat{\boldsymbol{\eta}} = \boldsymbol{\eta} + \mathbf{w}, \quad (12)$$

where $\mathbf{w} \sim \mathcal{N}(0, \sigma^2 \mathbf{I})$ represents the parameters estimation error, and $\boldsymbol{\eta}$ are the channel parameters of interest, given by

$$\boldsymbol{\eta} = [\psi_1^{\text{BM}}, \psi_2^{\text{BM}}, \psi_1^{\text{RM}}, \psi_2^{\text{RM}}, s_1^{\text{BM}}, s_2^{\text{BM}}, s_1^{\text{RM}}, s_2^{\text{RM}}, \omega_{\text{BM}}, \omega_{\text{BRM}}, b_{\text{BM}}, b_{\text{RM}}]. \quad (13)$$

Our proposed framework focuses on estimating the position and rotation angles of the MS. We aim to compare our results with the CRLB for the MS's position and orientation, referred to as the PEB and REB, respectively. The PEB and REB can be derived by differentiating the channel parameters PDF with respect to the parameter vector of interest [8], [9], given by $\boldsymbol{\zeta} = [x_{\text{M}}, y_{\text{M}}, z_{\text{M}}, \alpha_{\text{M}}, \beta_{\text{M}}, \gamma_{\text{M}}]$, as follows

$$\text{CRLB} = \mathbb{E} \left[-\frac{\partial^2 \ln p(\hat{\boldsymbol{\eta}}; \boldsymbol{\zeta})}{\partial \boldsymbol{\zeta}^2} \right]^{-1} = \left[\frac{1}{\sigma^2} \left\{ \frac{\partial \boldsymbol{\eta}}{\partial \boldsymbol{\zeta}} \frac{\partial \boldsymbol{\eta}^T}{\partial \boldsymbol{\zeta}} \right\} \right]^{-1}, \quad (14)$$

$$\text{PEB} = \sqrt{\text{tr}(\text{CRLB}_{1:3, 1:3})}, \quad \text{REB} = \sqrt{\text{tr}(\text{CRLB}_{4:6, 4:6})}, \quad (15)$$

the elements to compute (14) can be found in the Appendix.

IV. GRAPHICAL MODELS AND BAYESIAN INFERENCE

Bayesian networks are probabilistic graphical models that represent the joint probability distribution of a set of random variables through their conditional interdependencies. They utilize prior knowledge to infer the likelihood of events and make predictions. These networks are useful in solving localization problems by incorporating information about the system such as the channel model and error distributions.

Depicted as directed acyclic graphs (DAGs), Bayesian networks have vertices representing random variables and edges denoting its interdependencies [16]. In a DAG, each variable is conditionally independent of its non-descendants given its parents. This allows the joint probability density function (PDF) to be factorized, simplifying computations. For a DAG $\mathcal{D} = (V, E)$, the joint PDF of the random variables $X_v, v \in V$, where $\text{pa}(v)$ denotes the parents of v [17], is given by

$$p(V) = \prod_{v \in V} p(v | \text{pa}(v)). \quad (16)$$

When dealing with high-dimensional and complex distributions, finding the exact joint distribution that satisfies the model conditions can be difficult. Therefore, approximate inference methods like Markov chain Monte Carlo (MCMC)

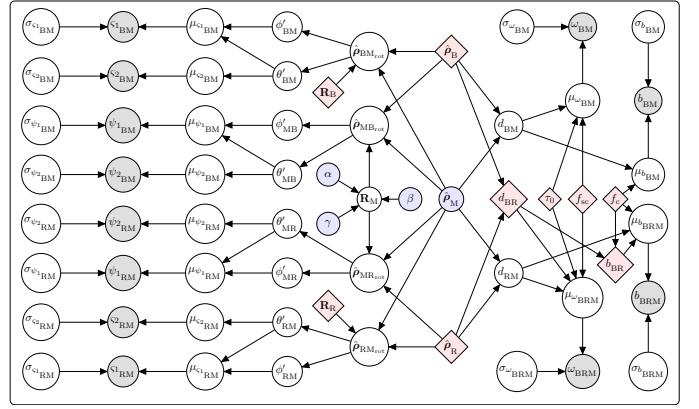


Fig. 2. Graphical model of the source localization.

are often employed. MCMC methods, based on Bayes's theorem, estimate the posterior distribution of model parameters to support the analysis and prediction [18]. These methods generate sequences of random samples to approximate target distributions. The No-U-Turn Sampler (NUTS) is an efficient MCMC method that avoids re-exploration and reduces simulation time by using a recursive algorithm to identify candidate points in the target distribution [19].

A. Localization Graphical Model

The directed acyclic graph model, shown in Fig. 2, represents our system. The parameters within the circles correspond to random variables whose distributions are derived from prior knowledge. The grey circles correspond to our observed data, and the blue color highlights the random variables of interest, which are the coordinates of the MS and its rotation given by α, β and γ . On the other hand, the red diamonds represent the known parameters, namely $\hat{\rho}_{\text{B}}, \hat{\rho}_{\text{R}}, d_{\text{BR}}, \mathbf{R}_{\text{B}}, \mathbf{R}_{\text{R}}, f_{\text{c}}, f_{\text{sc}}$ and τ_0 . These represent the coordinates of the BS, the coordinates of the RIS, the distance between the BS and RIS, the rotation matrix for the BS, the rotation matrix for the RIS, the central frequency, the subcarrier spacing, and the clock offset, respectively. These parameters are considered known by the system for all simulations.

The assumptions on the random variables' distribution constituting the respective Bayesian network are given in Table I, where \sim indicates that a random variable follows a specific distribution. We use a uniform distribution to initialize our prior knowledge of $(x_{\text{M}}, y_{\text{M}}, z_{\text{M}}, \alpha_{\text{M}}, \beta_{\text{M}}, \gamma_{\text{M}})$. This approach ensures that the sample space covers all the deployment scenario and possible rotations, once the target can be at any place of the environment with any rotation with same probability. The upper bound L is the side length of our deployment scenario, H is the height of the environment, and ϵ represents the maximum possible rotation angle. The covariance matrix for the observed data is given by Σ_{data} , where its main diagonal comprises a vector given by σ_{η}^2 , representing the variance of each observed data in (13). We model this variance with a small shape and scale in the inverse gamma distribution. This choice reduces the step size in the sampling process, simplifying the examination around the average.

TABLE I
RANDOM VARIABLES OF THE BAYESIAN NETWORK²

Variable	Description
x_M, y_M	$\sim \mathcal{U}(0, L)$
z_M	$\sim \mathcal{U}(0, H)$
$\alpha_M, \beta_M, \gamma_M$	$\sim \mathcal{U}(0, \epsilon)$
\mathbf{R}_M	$\sim \text{Equation (2)}$
d_{BM}	$\sim \ \hat{\rho}_B - \hat{\rho}_M\ $
d_{RM}	$\sim \ \hat{\rho}_R - \hat{\rho}_M\ $
$\hat{\rho}_{ij_{\text{rot}}}$	$\sim \mathbf{R}_j^T (\hat{\rho}_j - \hat{\rho}_i)$
θ'_{ij}	$\sim \arccos(\hat{\rho}_{ij_{\text{rot}}}[2])$
ϕ'_{ij}	$\sim \arctan 2(\hat{\rho}_{ij_{\text{rot}}}[1], \hat{\rho}_{ij_{\text{rot}}}[0])$
$\mu_{\psi 1_{\{BM, RM\}}}$	$\sim -\pi \sin(\theta'_{\{MB, MR\}}) \cos(\phi'_{\{MB, MR\}})$
$\mu_{\psi 2_{\{BM, RM\}}}$	$\sim -\pi \cos(\theta'_{\{MB, MR\}})$
$\mu_{\varsigma 1_{\{BM, RM\}}}$	$\sim -\pi \sin(\theta'_{\{BM, RM\}}) \cos(\phi'_{\{BM, RM\}})$
$\mu_{\varsigma 2_{\{BM, RM\}}}$	$\sim -\pi \cos(\theta'_{\{BM, RM\}})$
$\mu_{\omega_{BM}}$	$\sim -2\pi((d_{BM}/c) + \tau_0)f_{sc}$
$\mu_{\omega_{BRM}}$	$\sim -2\pi(((d_{BR} + d_{RM})/c) + \tau_0)f_{sc}$
$\mu_{b_{BM}}$	$\sim (c/f4\pi d_{BM})$
$\mu_{b_{BRM}}$	$\sim b_{BR}(c/f4\pi d_{RM})$
σ_η^2	$\sim \text{InverseGamma}(0.001, 0.001)$

V. SIMULATION RESULTS

In our simulations, we implement the indoor deployment scenario introduced in Section II. The scenario is a square area with a side length of 15 meters and 5 meters height, containing a RIS positioned at $\hat{\rho}_R = [7.5, 15, 4]^T$ and a base station at $\hat{\rho}_B = [0, 0, 5]^T$, both with known orientations. The channels are generated based on (5), where CE is applied to obtain near-perfect channel estimates, incorporating some estimation error as defined by (12). For efficiency, the orientation of the MS is constrained between 0 and $\pi/4$; orientations beyond this range would require a denser point sampling and thus increase simulation time. The localization estimator is implemented using the PyMC package [20], employing the NUTS algorithm to sample from the posterior distribution of coordinates and rotations. We feed NUTS with 50 data samples drawn from a Gaussian distribution, $\mathcal{N}(\hat{\eta}, \sigma_{sp}^2 \mathbf{I})$, based on the estimated parameters defined in (12) and $\sigma_{sp}^2 = 10^{-3}$ to reflect confidence on the CE accuracy. In each simulation run, NUTS operates with 4 chains, drawing 2500 samples per chain. The step size is tuned to 1500 to achieve an approximate sample acceptance rate of 90%. Targets are placed randomly within the simulated area, each assigned a random position and orientation.

The CDF for various values of CE error is illustrated in Fig. 3. The results are averaged over 30,000 simulation runs. In each iteration, the target assumes a different position and orientation, and the algorithm is fed with new samples. The black dotted line indicates the 90th percentile of the CDF, with its value is presented in Table II. This threshold indicates that

² $\mathcal{U}(l, u)$ represents a uniform distribution, where l is the lower bound and u is the upper bound, $\text{InverseGamma}(\alpha, \beta)$ represents a inverse gamma distribution, where α is the shape parameter and β the scale parameter, and ij are indices from a group $\mathcal{G} = \{(i, j) \in \{BM, MB, RM, MR\}\}$.

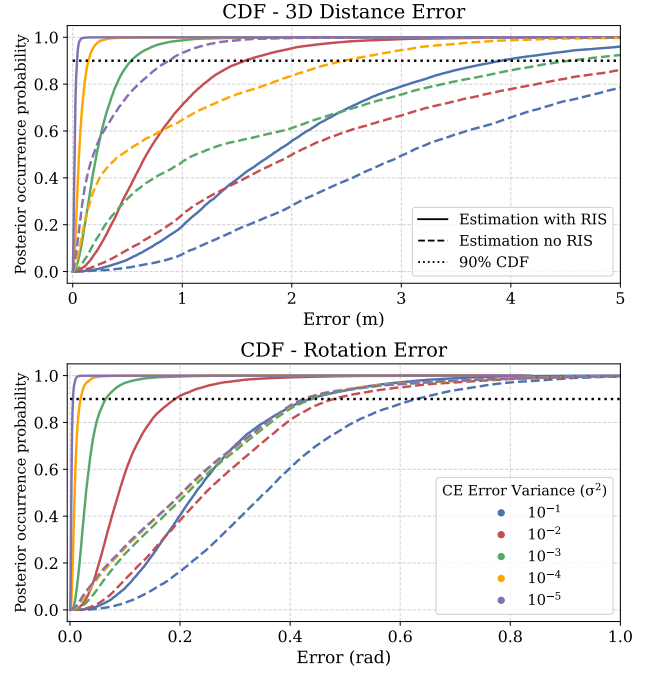


Fig. 3. CDF of the 6D error for the proposed source localization.

TABLE II
90% MARKER OF THE CDF VARYING THE CE ERROR VARIANCE.

Metric	Scenario	σ^2				
		10^{-1}	10^{-2}	10^{-3}	10^{-4}	10^{-5}
PEB (m)	RIS	3.91063	1.57071	0.53481	0.14384	0.03853
	No RIS	6.44283	5.55535	4.53914	2.47313	0.87843
REB (rad)	RIS	0.43547	0.19091	0.06510	0.01920	0.00547
	No RIS	0.63008	0.47993	0.43972	0.42581	0.42543

90% of the estimates are achieved with an error less than or equal to this value. The results show that scenarios without RIS shows lower accuracy in both position and rotation, compared to scenarios with RIS. The additional channel path provides more information about the target than simply relying on a LOS path. We observe a substantial improvement in rotation accuracy. Decreasing the error associated with the CE considerably increases the accuracy of the estimation of position and rotation in all scenarios. In cases with a lower CE error, such as $\sigma^2 = 10^{-3}$, and the presence of RIS, we observe an average error of 0.53 m in position and 0.06 rad in rotation, compared to 4.54 m and 0.44 rad without RIS.

Using the results from previous simulations, we calculate the PEB and REB in Fig. 4 and compare them with the theoretical bounds from (15). The results from scenarios with RIS are closely aligned with the bounds. Specifically, at low σ^2 values (e.g., below 10^{-2}), the PEB and REB in RIS-enabled scenarios are closely matching from the bounds. However, the same behavior does not apply in scenarios without RIS, where performance deviates from the bound. This difference occurs because, without the additional path provided by RIS, the algorithm lacks sufficient information to effectively estimate all the variables in the system. This limitation is particularly

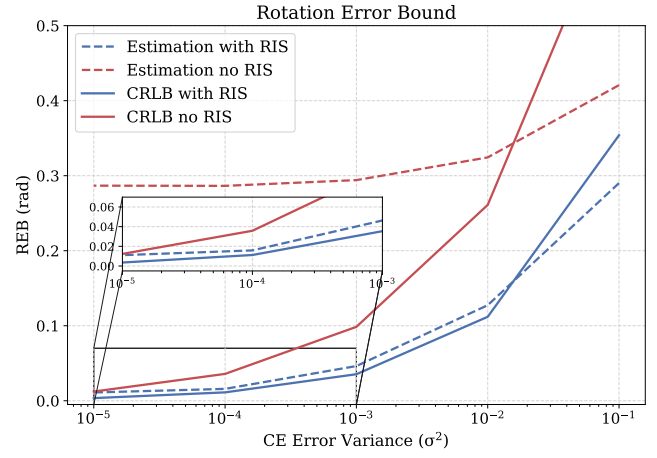
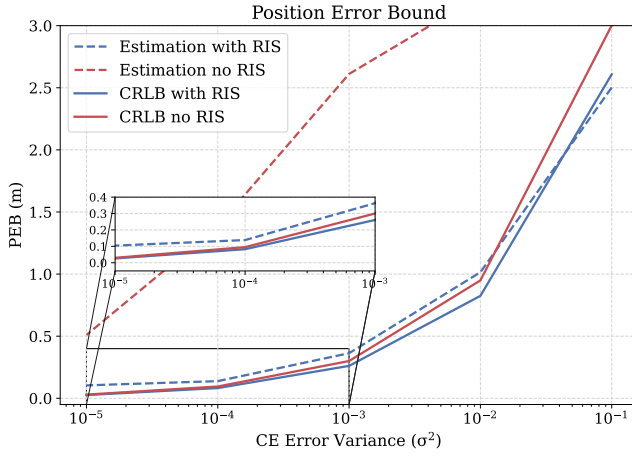


Fig. 4. PEB and REB for the proposed scenario varying the CE error variance.

evident in rotation estimation, where performance stabilizes around 0.3 rad, as the algorithm relies on guessing its rotation.

The presence of RIS significantly enhances parameter estimation by providing more information about the MS position and rotation. As shown in Fig. 4, our framework achieves near-perfect estimations, with position errors below 0.4 m and rotation errors below 0.05 rad when errors are below $\sigma^2 = 10^{-2}$. In high CE error scenarios, the performance of both scenarios is considerably degraded. Even with RIS, the high parameter error prevents the algorithm from reliably estimating position and rotation, leading it to rely on approximate guesses for rotation. This limitation may be mitigated by increasing the number of samples for the algorithm or the number of draws for NUTS. However, the approach would also increase processing time or complexity.

VI. CONCLUSIONS

We have developed a 6D Bayesian-based localization framework for estimating both position and rotation in an indoor RIS-aided environment. By utilizing a probabilistic graphical model and the NUTS, our approach accurately approximates the posterior distribution of localization parameters, using estimated channel parameters for improved precision. Through the derivation of the CRLB, we have quantified the system's accuracy with PEB and REB, setting it as a benchmark for evaluation. Our comparative analysis with scenarios without RIS highlights the performance improvements enabled by RIS, particularly in enhancing the accuracy of MS rotation estimation. This work demonstrates the potential of probabilistic graphical models and Bayesian methods for indoor localization problems, providing a robust framework that operates without the need for training, iterative learning, or multiple passes, achieving accurate estimates in a single snapshot. Future research directions include applying different CE algorithms to analyze their impact, exploring dynamic scenarios (e.g. iterative estimations for moving targets), examining the impact of multi-path components, and analyzing other data fusion techniques, such as visual data, to enhance and refine the proposed method.

ACKNOWLEDGMENT

The work was supported by the Research Council of Finland (former Academy of Finland) 6G Flagship Program (Grant Number: 346208). We also thank Prof. Mikko Sillanpää, Enrique Pinto, Hamza Djelouat, and Reijo Leinonen for the productive discussions.

APPENDIX A CRLB DERIVATION

To derive the CRLB in (14), we need to compute $\frac{\partial \eta}{\partial \zeta}$. By using (7), (8), (9) and (10), along with the parameter relationships given by (3), (3) and (4), the elements of the CRLB can be computed. Before deriving the parameters, we first introduce the following auxiliary variables

$$\chi_{BM} \triangleq \hat{\rho}_M - \hat{\rho}_B, \chi_{RM} \triangleq \hat{\rho}_M - \hat{\rho}_R, d_{BM} \triangleq \|\hat{\rho}_M - \hat{\rho}_B\| \quad (17)$$

$$d_{RM} \triangleq \|\hat{\rho}_M - \hat{\rho}_R\|, \mathbf{K}_{MB} = \mathbf{R}_M \frac{\chi_{BM}}{d_{BM}}, \mathbf{K}_{MR} = \mathbf{R}_M \frac{\chi_{RM}}{d_{RM}}, \quad (18)$$

$$\mathbf{K}_{BM} = \mathbf{R}_B \frac{\chi_{BM}}{d_{BM}} \text{ and } \mathbf{K}_{RM} = \mathbf{R}_R \frac{\chi_{RM}}{d_{RM}}, \quad (19)$$

as well $\mathbf{u}_1 \triangleq [1, 0, 0]^T$, $\mathbf{u}_2 \triangleq [0, 1, 0]^T$ and $\mathbf{u}_3 \triangleq [0, 0, 1]^T$, to rewrite (4) as

$$\theta'_{MB} = \arccos(\mathbf{u}_3^T \mathbf{K}_{MB}), \phi'_{MB} = \arctan 2(\mathbf{u}_2^T \mathbf{K}_{MB}, \mathbf{u}_1^T \mathbf{K}_{MB}), \quad (20)$$

$$\theta'_{MR} = \arccos(\mathbf{u}_3^T \mathbf{K}_{MR}), \phi'_{MR} = \arctan 2(\mathbf{u}_2^T \mathbf{K}_{MR}, \mathbf{u}_1^T \mathbf{K}_{MR}), \quad (21)$$

$$\theta'_{BM} = \arccos(\mathbf{u}_3^T \mathbf{K}_{BM}), \phi'_{BM} = \arctan 2(\mathbf{u}_2^T \mathbf{K}_{BM}, \mathbf{u}_1^T \mathbf{K}_{BM}), \quad (22)$$

$$\theta'_{RM} = \arccos(\mathbf{u}_3^T \mathbf{K}_{RM}), \phi'_{RM} = \arctan 2(\mathbf{u}_2^T \mathbf{K}_{RM}, \mathbf{u}_1^T \mathbf{K}_{RM}). \quad (23)$$

Then we have the following derivatives:

$$\frac{\partial \theta'_{MB}}{\partial \hat{\rho}_M} = \frac{-\mathbf{u}_3^T \mathbf{R}_M (-\mathbf{A}_{BM})}{\sqrt{1 - (\mathbf{u}_3^T \mathbf{K}_{MB})^2}}, \frac{\partial \theta'_{MR}}{\partial \hat{\rho}_M} = \frac{-\mathbf{u}_3^T \mathbf{R}_M (-\mathbf{A}_{RM})}{\sqrt{1 - (\mathbf{u}_3^T \mathbf{K}_{MR})^2}}, \quad (24)$$

$$\frac{\partial \theta'_{BM}}{\partial \hat{\rho}_M} = \frac{-\mathbf{u}_3^T \mathbf{R}_B \mathbf{A}_{BM}}{\sqrt{1 - (\mathbf{u}_3^T \mathbf{K}_{BM})^2}}, \frac{\partial \theta'_{RM}}{\partial \hat{\rho}_M} = \frac{-\mathbf{u}_3^T \mathbf{R}_R \mathbf{A}_{RM}}{\sqrt{1 - (\mathbf{u}_3^T \mathbf{K}_{RM})^2}}, \quad (25)$$

$$\frac{\partial \phi'_{\{MB, MR\}}}{\partial \hat{\rho}_M} = \frac{\mathbf{u}_1^T \mathbf{K}_{\{MB, MR\}} (\mathbf{R}_M^T \mathbf{u}_2)^T (-\mathbf{A}_{\{BM, RM\}})}{\mathbf{u}_1^T \mathbf{K}_{\{MB, MR\}}^2 + \mathbf{u}_2^T \mathbf{K}_{\{MB, MR\}}^2} - \frac{\mathbf{u}_2^T \mathbf{K}_{\{MB, MR\}} (\mathbf{R}_M^T \mathbf{u}_1)^T (-\mathbf{A}_{\{BM, RM\}})}{\mathbf{u}_1^T \mathbf{K}_{\{MB, MR\}}^2 + \mathbf{u}_2^T \mathbf{K}_{\{MB, MR\}}^2}, \quad (26)$$

$$\frac{\partial \phi'_{\{BM, RM\}}}{\partial \hat{\rho}_M} = \frac{\mathbf{u}_1^T \mathbf{K}_{\{BM, RM\}} (\mathbf{R}_{\{B, R\}}^T \mathbf{u}_2)^T \mathbf{A}_{\{BM, RM\}}}{\mathbf{u}_1^T \mathbf{K}_{\{BM, RM\}}^2 + \mathbf{u}_2^T \mathbf{K}_{\{BM, RM\}}^2} - \frac{\mathbf{u}_2^T \mathbf{K}_{\{BM, RM\}} (\mathbf{R}_{\{B, R\}}^T \mathbf{u}_1)^T \mathbf{A}_{\{BM, RM\}}}{\mathbf{u}_1^T \mathbf{K}_{\{BM, RM\}}^2 + \mathbf{u}_2^T \mathbf{K}_{\{BM, RM\}}^2}, \quad (27)$$

$$\frac{\partial \psi'_{MB}}{\partial \mathbf{r}_M} = \frac{-\mathbf{u}_3^T \frac{\partial \mathbf{R}_M}{\partial \mathbf{r}_M} \left(\frac{-\chi_{BM}}{d_{BM}} \right)}{\sqrt{1 - (\mathbf{u}_3^T \mathbf{K}_{MB})^2}}, \quad \frac{\partial \theta'_{MR}}{\partial \mathbf{r}_M} = \frac{-\mathbf{u}_3^T \frac{\partial \mathbf{R}_M}{\partial \mathbf{r}_M} \left(\frac{-\chi_{RM}}{d_{RM}} \right)}{\sqrt{1 - (\mathbf{u}_3^T \mathbf{K}_{MR})^2}}, \quad (28)$$

$$\frac{\partial \phi'_{\{MB, MR\}}}{\partial \mathbf{r}_M} = \frac{\mathbf{u}_1^T \mathbf{K}_{\{MB, MR\}} \mathbf{u}_2^T \frac{\partial \mathbf{R}_M}{\partial \mathbf{r}_M} \left(\frac{-\chi_{\{MB, MR\}}}{d_{\{MB, MR\}}} \right)}{\mathbf{u}_1^T \mathbf{K}_{\{MB, MR\}}^2 + \mathbf{u}_2^T \mathbf{K}_{\{MB, MR\}}^2} - \frac{\mathbf{u}_2^T \mathbf{K}_{\{MB, MR\}} \mathbf{u}_1^T \frac{\partial \mathbf{R}_M}{\partial \mathbf{r}_M} \left(\frac{-\chi_{\{MB, MR\}}}{d_{\{MB, MR\}}} \right)}{\mathbf{u}_1^T \mathbf{K}_{\{MB, MR\}}^2 + \mathbf{u}_2^T \mathbf{K}_{\{MB, MR\}}^2}, \quad (29)$$

$$\frac{\partial \theta'_{BM}}{\partial \mathbf{r}_M} = \frac{\partial \theta'_{RM}}{\partial \mathbf{r}_M} = \frac{\partial \phi'_{BM}}{\partial \mathbf{r}_M} = \frac{\partial \phi'_{RM}}{\partial \mathbf{r}_M} = 0, \quad (30)$$

where

$$\mathbf{A}_{\{BM, RM\}} = \frac{\mathbf{I}_3}{d_{\{BM, RM\}}} - \frac{\chi_{\{BM, RM\}}^T \otimes \chi_{\{BM, RM\}}}{d_{\{BM, RM\}}^{3/2}}, \quad (31)$$

$$\frac{\partial \mathbf{R}_M}{\partial \alpha_M} = \frac{\partial \mathbf{R}_z(\alpha_M)}{\partial \alpha_M} \mathbf{R}_y(\beta_M) \mathbf{R}_x(\gamma_M), \quad (32)$$

$$\frac{\partial \mathbf{R}_M}{\partial \beta_M} = \mathbf{R}_z(\alpha_M) \frac{\partial \mathbf{R}_y(\beta_M)}{\partial \beta_M} \mathbf{R}_x(\gamma_M), \quad (33)$$

$$\frac{\partial \mathbf{R}_M}{\partial \gamma_M} = \mathbf{R}_z(\alpha_M) \mathbf{R}_y(\beta_M) \frac{\partial \mathbf{R}_x(\gamma_M)}{\partial \gamma_M}, \quad (34)$$

$$\frac{\partial \mathbf{R}_z(\alpha_M)}{\partial \alpha_M} = \begin{bmatrix} -\sin(\alpha) & -\cos(\alpha) & 0 \\ \cos(\alpha) & -\sin(\alpha) & 0 \\ 0 & 0 & 0 \end{bmatrix}, \quad (35)$$

$$\frac{\partial \mathbf{R}_y(\beta_M)}{\partial \beta_M} = \begin{bmatrix} -\sin(\beta) & 0 & \cos(\beta) \\ 0 & 0 & 0 \\ -\cos(\beta) & 0 & -\sin(\beta) \end{bmatrix}, \quad (36)$$

$$\frac{\partial \mathbf{R}_x(\gamma_M)}{\partial \gamma_M} = \begin{bmatrix} 0 & 0 & 0 \\ 0 & -\sin(\gamma) & -\cos(\gamma) \\ 0 & \cos(\gamma) & -\sin(\gamma) \end{bmatrix}. \quad (37)$$

The latter expressions are used to compute the following elements:

$$\frac{\partial \psi_1^{\{BM, RM\}}}{\partial \hat{\rho}_M} = \frac{\partial \psi_1^{\{BM, RM\}}}{\partial \theta'_{\{MB, MR\}}} \frac{\partial \theta'_{\{MB, MR\}}}{\partial \hat{\rho}_M} - \frac{\partial \psi_1^{\{BM, RM\}}}{\partial \phi'_{\{MB, MR\}}} \frac{\partial \phi'_{\{MB, MR\}}}{\partial \hat{\rho}_M}, \quad (38)$$

$$\frac{\partial \psi_2^{\{BM, RM\}}}{\partial \hat{\rho}_M} = \frac{\partial \psi_2^{\{BM, RM\}}}{\partial \theta'_{\{MB, MR\}}} \frac{\partial \theta'_{\{MB, MR\}}}{\partial \hat{\rho}_M}, \quad (39)$$

$$\frac{\partial \varsigma_1^{\{BM, RM\}}}{\partial \hat{\rho}_M} = \frac{\partial \varsigma_1^{\{BM, RM\}}}{\partial \theta'_{\{BM, RM\}}} \frac{\partial \theta'_{\{BM, RM\}}}{\partial \hat{\rho}_M} - \frac{\partial \varsigma_1^{\{BM, RM\}}}{\partial \phi'_{\{BM, RM\}}} \frac{\partial \phi'_{\{BM, RM\}}}{\partial \hat{\rho}_M}, \quad (40)$$

$$\frac{\partial \varsigma_2^{\{BM, RM\}}}{\partial \hat{\rho}_M} = \frac{\partial \varsigma_2^{\{BM, RM\}}}{\partial \theta'_{\{BM, RM\}}} \frac{\partial \theta'_{\{BM, RM\}}}{\partial \hat{\rho}_M}, \quad (41)$$

$$\frac{\partial \omega_{\{BM, BRM\}}}{\partial \hat{\rho}_M} = \frac{-2\pi f_{sc}}{d_{\{BM, RM\}} c} \mathbf{I}_3 \chi_{\{BM, RM\}}, \quad (42)$$

$$\frac{\partial b_{BM}}{\partial \hat{\rho}_M} = \frac{-c \mathbf{I}_3 \chi_{BM}}{4\pi f(d_{BM})^3}, \quad \frac{\partial b_{BRM}}{\partial \hat{\rho}_M} = \frac{-b_{BR} c \mathbf{I}_3 \chi_{RM}}{4\pi f(d_{RM})^3}, \quad (43)$$

$$\frac{\partial \psi_1^{\{BM, RM\}}}{\partial \mathbf{r}_M} = \frac{\partial \psi_1^{\{BM, RM\}}}{\partial \theta'_{\{MB, MR\}}} \frac{\partial \theta'_{\{MB, MR\}}}{\partial \mathbf{r}_M} - \frac{\partial \psi_1^{\{BM, RM\}}}{\partial \phi'_{\{MB, MR\}}} \frac{\partial \phi'_{\{MB, MR\}}}{\partial \mathbf{r}_M}, \quad (44)$$

$$\frac{\partial \psi_2^{\{BM, RM\}}}{\partial \mathbf{r}_M} = \frac{\partial \psi_2^{\{BM, RM\}}}{\partial \theta'_{\{MB, MR\}}} \frac{\partial \theta'_{\{MB, MR\}}}{\partial \mathbf{r}_M}, \quad \frac{\partial \varsigma_1^{\{BM, RM\}}}{\partial \mathbf{r}_M} = \frac{\partial \varsigma_2^{\{BM, RM\}}}{\partial \mathbf{r}_M} = 0, \quad (45)$$

$$\frac{\partial \omega_{\{BM, BRM\}}}{\partial \mathbf{r}_M} = \frac{\partial b_{BM}}{\partial \mathbf{r}_M} = \frac{\partial b_{BRM}}{\partial \mathbf{r}_M} = 0. \quad (46)$$

REFERENCES

- [1] Y. Liu, X. Liu, X. Mu, T. Hou, J. Xu, M. Di Renzo, and N. Al-Dhahir, "Reconfigurable intelligent surfaces: Principles and opportunities," *IEEE Commun. Surveys & Tutorials*, vol. 23, no. 3, pp. 1546–1577, 2021.
- [2] R. Chen, M. Liu, Y. Hui, N. Cheng, and J. Li, "Reconfigurable intelligent surfaces for 6G IoT wireless positioning: A contemporary survey," *IEEE Internet of Things J.*, vol. 9, no. 23, pp. 23 570–23 582, 2022.
- [3] Q. Wu and R. Zhang, "Towards smart and reconfigurable environment: Intelligent reflecting surface aided wireless network," *IEEE Commun. Mag.*, vol. 58, no. 1, pp. 106–112, 2019.
- [4] A. Behravan, V. Yajnanarayana, M. F. Keskin, H. Chen, D. Shrestha, T. E. Abruđan, T. Svensson, K. Schindhelm, A. Wolfgang, S. Lindberg *et al.*, "Positioning and sensing in 6g: Gaps, challenges, and opportunities," *IEEE Veh. Technol. Mag.*, 2022.
- [5] B. Zheng, C. You, W. Mei, and R. Zhang, "A survey on channel estimation and practical passive beamforming design for intelligent reflecting surface aided wireless communications," *IEEE Commun. Surveys & Tutorials*, vol. 24, no. 2, pp. 1035–1071, 2022.
- [6] M. Bayraktar, J. Palacios, N. González-Prelcic, and C. J. Zhang, "Multidimensional orthogonal matching pursuit-based ris-aided joint localization and channel estimation at mmwave," in *Proc. IEEE Works. on Sign. Proc. Adv. in Wirel. Comms.*, 2022, pp. 1–5.
- [7] X. Wei, D. Shen, and L. Dai, "Channel estimation for ris assisted wireless communications—part i: Fundamentals, solutions, and future opportunities," *IEEE Commun. Lett.*, vol. 25, no. 5, pp. 1398–1402, 2021.
- [8] R. Ghazalian, G. C. Alexandropoulos, G. Seco-Granados, H. Wymeersch, and R. Jantti, "Joint 3d user and 6d hybrid reconfigurable intelligent surface localization," *IEEE Trans. Veh. Technol.*, 2024.
- [9] Y. Liu, S. Hong, C. Pan, Y. Wang, Y. Pan, and M. Chen, "Cramér-rao lower bound analysis of multiple-ris-aided mmwave positioning systems," in *Proc. IEEE Int. Symp. Pers., Indoor, Mobile Radio Commun.*, 2022, pp. 1110–1115.
- [10] Y. Zhang, Y. Liu, Y. Liu, L. Wu, Z. Zhang, and J. Dang, "Multi-ris-assisted millimeter wave single base station localization," in *4th Information Communication Technologies Conference (ICTC)*. IEEE, 2023, pp. 115–120.
- [11] 3GPP, "Study on channel model for frequencies from 0.5 to 100 GHz," 3rd Generation Partnership Project (3GPP), Technical Specification (TS) 38.901, 2020, version 16.1.0. [Online]. Available: <https://portal.3gpp.org>
- [12] J. He, A. Fakhreddine, and G. C. Alexandropoulos, "Simultaneous indoor and outdoor 3d localization with star-ris-assisted millimeter wave systems," in *Proc. IEEE Veh. Technol. Conf.*, 2022, pp. 1–6.
- [13] J. An, C. Yuen, Y. L. Guan, M. Di Renzo, M. Debbah, H. V. Poor, and L. Hanzo, "Two-dimensional direction-of-arrival estimation using stacked intelligent metasurfaces," *IEEE J. Select. Areas Commun.*, 2024.
- [14] M. Bayraktar, N. González-Prelcic, G. C. Alexandropoulos, and H. Chen, "Ris-aided joint channel estimation and localization at mmwave under hardware impairments: A dictionary learning-based approach," *IEEE Trans. Wireless Commun.*, 2024.
- [15] C. Huang, G. C. Alexandropoulos, C. Yuen, and M. Debbah, "Indoor signal focusing with deep learning designed reconfigurable intelligent surfaces," in *Proc. IEEE Works. on Sign. Proc. Adv. in Wirel. Comms.* IEEE, 2019, pp. 1–5.
- [16] S. L. Lauritzen, *Graphical models*. Clarendon Press, 1996, vol. 17.
- [17] D. Koller and N. Friedman, *Probabilistic graphical models: principles and techniques*. MIT press, 2009.
- [18] N. Metropolis and S. Ulam, "The monte carlo method," *Journal of the American statistical association*, vol. 44, no. 247, pp. 335–341, 1949.
- [19] M. D. Hoffman, A. Gelman *et al.*, "The No-U-Turn sampler: adaptively setting path lengths in Hamiltonian Monte Carlo." *J. Mach. Learn. Res.*, vol. 15, no. 1, pp. 1593–1623, 2014.
- [20] A.-P. Oriol, A. Virgile *et al.*, "PyMC: A modern and comprehensive probabilistic programming framework in python," *PeerJ Computer Science*, vol. 9, p. e1516, 2023.